

# MESOSCALE FORECAST ANALYSIS OF ATMOSPHERIC BOUNDARY LAYER STRUCTURE AND ELECTROMAGNETIC SIGNAL ATTENUATION DURING THE TERRAIN-INDUCED ROTOR EXPERIMENT (T-REX)

E. Colón\*

Network Computing Services, Inc. / Army High Performance Research Center  
Adelphi, Maryland, 20783

R.E. Dumais, T. Henmi, and R. Flanigan

Army Research Laboratory / Battlefield Environment Division  
White Sands Missile Range, New Mexico, 88002

## ABSTRACT

With the increased importance of high bandwidth microwave communication and remote sensing capabilities in Army battlefield operations, the need arises in being able to quantify the impact of microwave signal attenuation sources such as turbulence-driven fluctuations in the atmospheric refractive index and gaseous absorption. An assessment of attenuation effects in the atmospheric boundary layer was afforded by the Terrain-Induced Rotor Experiment (T-REX), which was a large-scale, observational study involving participants from several research agencies and academic institutions with the goal of examining the structure and evolution of atmospheric rotors and waves that develop over regions of complex terrain. A statistical analysis is presented in which the forecast accuracy of the Weather Research and Forecasting (WRF) Advance Research WRF (ARW) model employed by the Army Research Laboratory's Battlefield Environment Division is quantified using data collected from the Integrated Sounding System (ISS) Multiple Antenna Profiler Radar (MAPR) during T-REX Intensive Observation Periods (IOPs). It was found that vertical profiles of attenuation fields obtained from both model and observational sources were strongly correlated for gaseous absorption contributions but only a weak statistical relationship exists for scintillation contributions. This outcome suggests that mesoscale numerical weather prediction (NWP) models that are run at high spatial resolutions may potentially be used to generate forecasts that are tailored towards predicting EM attenuation effects over battlefield environments.

## 1. INTRODUCTION

The portion of the atmosphere which has the greatest impact on Army ground operations is the layer that extends from the surface to ~0.5 - 2 kilometers above ground level and is designated the atmospheric boundary layer (ABL). Exchanges of heat, moisture, and momentum occur between the Earth's surface and the atmosphere through the ABL on timescales of minutes to

hours. The vertical mixing of heat, moisture, and momentum fluxes is facilitated by stochastic, 3-dimensional fluctuations in atmospheric flow (turbulence) that manifested as transient eddies in meteorological fields such as wind speed and direction (Kaimal and Finnigan, 1994). The intensity of these turbulent eddies across a range of spatial and temporal scales characterizes the instantaneous state of the ABL. It has been demonstrated, in a number of observational and modeling studies, that atmospheric turbulence may have a significantly impact on the propagation of electromagnetic (EM) waves at transmitting frequencies that are commonly used in communication and remote sensing applications (David, 2004; Kravtsov, 1992; Bohlander et al., 1988; Ishimaru, 1978).

As an EM wave traverses a turbulent layer of the atmosphere, its intensity may be reduced by fluctuations in the atmosphere's index of refraction known as scintillations. Scintillations not only reduce an EM signal's effective range over large distances but may also alter the phase of the propagating wave leading to changes in the angle-of-arrival that a wave front makes with its intended target (Bohlander et al., 1988). The latter effect is particularly important in remote sensing applications such as radar targeting since it may introduce tracking errors that fall outside of the error budget allotted for high precision systems (Hill et al., 1988; Bohlander et al., 1988). To ascertain the impact of scintillations on EM wave propagation conditions in the ABL, accurate estimates of the atmospheric refractive index ( $n$ ), and the refractive index structure parameter,  $C_n^2$ , are needed. This requirement is addressed in Section 3 which describes how EM signal attenuation due to scintillations ( $A_{Cn2}$ ) can be derived from  $n$  and  $C_n^2$  which, in turn, are calculated using NWP model forecast products.

Another important source of attenuation that is considered in this study is gaseous absorption due to atmospheric oxygen ( $A_{O2}$ ) and water vapor ( $A_{H2O}$ ). These atmospheric constituents strongly dampen the intensity of EM signals that fall within a frequency range of 1 –

Report Documentation Page				Form Approved OMB No. 0704-0188	
Public reporting burden for the collection of information is estimated to average 1 hour per response, including the time for reviewing instructions, searching existing data sources, gathering and maintaining the data needed, and completing and reviewing the collection of information. Send comments regarding this burden estimate or any other aspect of this collection of information, including suggestions for reducing this burden, to Washington Headquarters Services, Directorate for Information Operations and Reports, 1215 Jefferson Davis Highway, Suite 1204, Arlington VA 22202-4302. Respondents should be aware that notwithstanding any other provision of law, no person shall be subject to a penalty for failing to comply with a collection of information if it does not display a currently valid OMB control number.					
1. REPORT DATE <b>01 NOV 2006</b>		2. REPORT TYPE <b>N/A</b>		3. DATES COVERED <b>-</b>	
4. TITLE AND SUBTITLE <b>Mesoscale Forecast Analysis of Atmospheric Boundary Layer Structure and Electromagnetic Signal Attenuation During the Terrain-Induced Rotor Experiment (T-REX)</b>				5a. CONTRACT NUMBER	
				5b. GRANT NUMBER	
				5c. PROGRAM ELEMENT NUMBER	
6. AUTHOR(S)				5d. PROJECT NUMBER	
				5e. TASK NUMBER	
				5f. WORK UNIT NUMBER	
7. PERFORMING ORGANIZATION NAME(S) AND ADDRESS(ES) <b>Network Computing Services, Inc. / Army High Performance Research Center Adelphi, Maryland, 20783</b>				8. PERFORMING ORGANIZATION REPORT NUMBER	
9. SPONSORING/MONITORING AGENCY NAME(S) AND ADDRESS(ES)				10. SPONSOR/MONITOR'S ACRONYM(S)	
				11. SPONSOR/MONITOR'S REPORT NUMBER(S)	
12. DISTRIBUTION/AVAILABILITY STATEMENT <b>Approved for public release, distribution unlimited</b>					
13. SUPPLEMENTARY NOTES <b>See also ADM002075., The original document contains color images.</b>					
14. ABSTRACT					
15. SUBJECT TERMS					
16. SECURITY CLASSIFICATION OF:			17. LIMITATION OF ABSTRACT <b>UU</b>	18. NUMBER OF PAGES <b>26</b>	19a. NAME OF RESPONSIBLE PERSON
a. REPORT <b>unclassified</b>	b. ABSTRACT <b>unclassified</b>	c. THIS PAGE <b>unclassified</b>			

1000 GHz. Absorption coefficients for each molecular species are largely a function of the absorbing gases' abundance, pressure and the EM signal's frequency. These coefficients have been calculated using radiative transfer models (Smith, 1982) and curve-fitting techniques applied to retrieved atmospheric brightness temperature data (ITU-R P.676).

Quantifying the skill with which we can predict EM signal attenuations within the ABL due to scintillations and gaseous absorption is our goal. Section 2 of this paper describes the implementation of WRF ARW (Skamarock et al., 2005) model in support of the T-REX field campaign (Grubisic et al., 2004). Attenuation models are characterized in Section 3 with an emphasis on how contributions may be derived from prognostically determined meteorological variables. Furthermore, statistical comparisons are presented based on WRF ARW forecast products and measurement data for a specific IOP and all IOPs combined. A conclusion summarizes our findings and discusses future work that is needed in order to fully develop our approach in producing accurate, high resolution, EM signal propagation forecasts for battlefield environments.

## 2. WRF-ARW AND T-REX

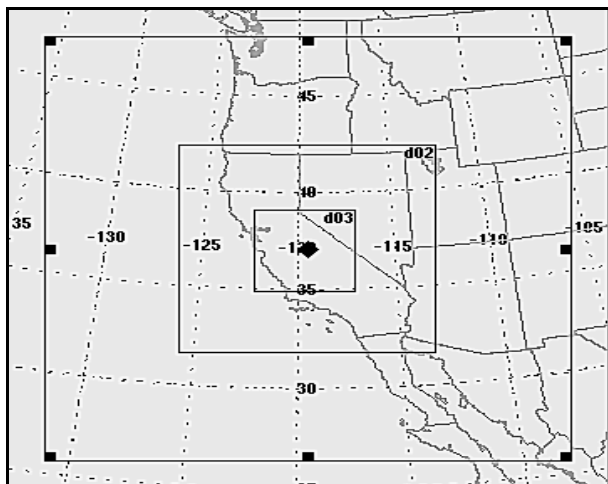


Fig. 1. WRF-ARW nested domains centered over Owens Valley, California (37.1°N, 119.5°W).

Held between late February and early May of 2006, T-REX provided an ideal case study for examining the structure of the ABL over a region where local weather is continuously influenced by wind shear-driven turbulence. Data collected from a number of sources including radiosondes, dropsondes, automated weather stations, lidars, and radar profilers, among others, has thus far proven to be invaluable in examining the interaction between terrain, mountain wave development

and atmospheric dynamics. To take advantage of this data rich environment, in terms of forecast validation, a collaborative effort between the Army Research Laboratory / Battlefield Environment Division (ARL/BED) and the Army High Performance Computing Research Center (AHPARC) evolved with the goal of implementing WRF ARW to produce high resolution forecasts over the T-REX domain. Several other agencies and academic institutions also produced near-real time forecast products using different mesoscale NWP models. The combined weather forecasting effort served as the predictive component of the T-REX field campaign.

The WRF ARW model employed by ARL/BED/AHPARC was initialized using a "cold start" condition with Global Forecasting System (GFS) (Campana et al., 1994) 0.5 degree resolution data. Simulations were initiated at 12 Z (4 a.m. local time for Owens Valley, California) using daily 06 Z GFS data. Model output was produced on an hourly cycle for a total of 48 hours starting from the 12Z initialization time for each field campaign day. Forecast products were generated daily from 12Z February 28, 2006 to 12Z May 2, 2006 for a total of 62 overlapping 48-hour cycles. The AHPARC Cray X1E platform served as the primary high performance computing resource during T-REX. Its vector processor architecture is well suited to handling large problem sizes encountered in mesoscale NWP modeling (Meys, 2002). A total of 32 multi-streaming processors (MSPs) were employed in each daily forecast cycle with pre- and post-processing duties handled on the same platform but using a single MSP per task.

The model's domain configuration was developed using the WRF Standard Initialization (WRFSI) utility and is based on the scheme employed by the Naval Research Laboratory's Coupled Ocean-Atmosphere Modeling Prediction System (COAMPS) (Hodur, 1997). Fig. 1 depicts the horizontal arrangement of nested domains utilized in this scheme. The outermost domain was composed of 91 X 91 grid elements with a resolution of 18 km per grid spacing. The first nested domain was composed of 157 X 157 grid elements with a 6 km resolution and the second nested (innermost) domain was composed of 133 X 133 grid elements with a resolution of 2 km. All domains were centered on the same coordinate (37.1°N, 119.5°W) so that individual grid points were coincident across the entire T-REX regime. There were 40 vertical  $\sigma$  levels defined in each domain which were distributed from the model surface to a 10 hPa model top. In an effort to maintain a high vertical resolution within the ABL, 23 of 40 levels are concentrated within the bottom 20% of the model atmosphere. The terrain data set used to define the lower model boundary originated from the 30 arcsecond resolution, United States Geological Survey (USGS)

topography products as prescribed using WRFSI. Fig. 2 highlights the topography of the innermost WRF-ARW T-REX domain (which was used in our statistical analysis) in which the Owens Valley depression is evident as a light shaded band stretching from the northwest to the south of the domain. The Sierra Madre mountain chain borders Owens Valley to the west and the White and Inyo mountains border Owens Valley to the east. The location of Independence, California is delineated by a star located near the center of the Owens Valley basin.

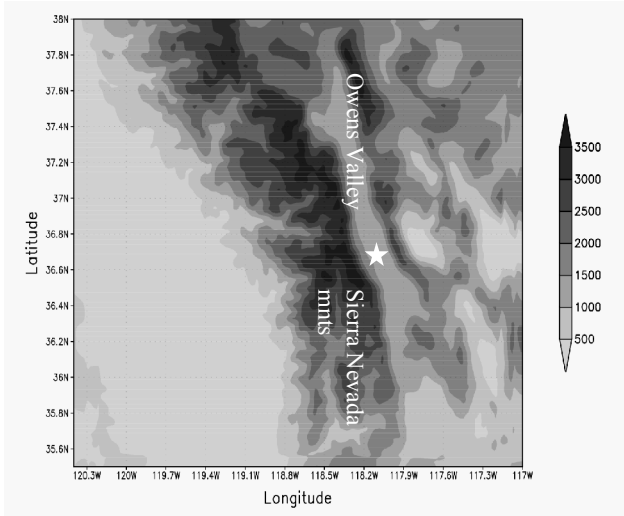


Fig. 2. Terrain elevation in m above sea level (ASL) coinciding with the inner-most WRF-ARW T-REX domain where the star coincides with the location of Independence, California.

Conventional model physics parameterizations were used in this study and are highlighted in Table 1. The only change in the schemes employed between nested domains was in the resolution-dependent time step and cumulus physics parameterizations. Below a resolution of 5 km, WRF ARW is able to spatially resolve cumulus convective systems so that the Kain-Fritsch Eta cumulus physics parameterization is deactivated in the innermost domain. Selecting an appropriate time step for all three domains involved preserving the 3:1 ratio utilized in scaling of horizontal domain resolutions. However, the traditional 5 seconds-per-1-kilometer-resolution ratio enabled by the use of a 3<sup>rd</sup> order Runge Kutta time splitting scheme (Skamarock et al., 2005) proved inadequate in handling the steep terrain gradients encountered between the Sierra Madre mountains and the Owens Valley basin which are among the steepest in the continental US (Grubisic et al., 2004). It was found that a time step to horizontal resolution ratio of 3:1 instead of 5:1 avoided the numerical instabilities that would develop near abrupt terrain features.

Table 1. Model Configuration

Physics scheme/parameterization	WRF-ARW
Microphysics	Lin et al.
Cumulus physics	Kain-Fritsch scheme
Shortwave radiation	Dudhia scheme
Longwave radiation	Rrtm scheme
Land surface model	NOAH model
ABL/surface similarity scheme	YSU scheme
Surface layer physics	Monin-Obukhov scheme
Time step-to-resolution ratio	3:1
Domain nesting ratio	3:1
Nesting scheme	Interactive

### 3. EM SIGNAL ATTENUATION

We will now examine how WRF ARW prognostic fields were used to estimate attenuation contributions and how the resulting attenuations compared with data derived from observations. To address gaseous absorption, we used the model described in ITU-R P.676-6 in which specific attenuation spectra were generated by summing contributions from individual water vapor and oxygen absorption lines at specific pressure levels (Smith, 1982). Within this scheme, water vapor attenuation contributions are dependent on EM signal frequency, water vapor partial pressure and water vapor density. Oxygen attenuation spectra, on the other hand, are dependent on EM signal frequency and oxygen partial pressure. Since both total atmospheric pressure and water vapor mixing ratio are WRF ARW prognostic variables, deriving estimates of gaseous attenuation contributions from these gaseous species is a straight forward procedure (Hodges et al., 2006).

The scintillation contribution to EM signal attenuation is dependent on a number of factors including the refractive index structure parameter  $C_n^2$ . As its name implies, it is directly dependent on the atmosphere's index of refraction and can be formulated, in Cartesian coordinates (x, y, z, t), as:

$$n(x, y, z, t) = C \cdot \frac{p(x, y, z, t)}{\theta(x, y, z, t)} + C_w \cdot \frac{e(x, y, z, t)}{\theta(x, y, z, t)^2}, \quad (1)$$

where  $C = 7.76 \times 10^{-7} \text{ K Pa}^{-1}$ ,  $C_w = 3.73 \times 10^{-3} \text{ K}^2 \text{ Pa}^{-1}$ ,  $p(x, y, z, t)$  is total atmospheric pressure,  $\theta(x, y, z, t)$  is potential temperature, and  $e(x, y, z, t)$  is water vapor partial pressure. The most direct approach in deriving  $C_n^2$  is diagnostically from (1) as follows (Muschinski et al., 1999):

$$C_n^2(x, y, z, t) = \frac{[n(x, y, z + \Delta z/2, t) - n(x, y, z - \Delta z/2, t)]^2}{\Delta z^{2/3}}, \quad (2)$$

where  $\Delta z$  is the model's vertical grid spacing. We may compute  $C_n^2(x, y, z, t)$  along any of the Cartesian directions but have chosen to use the vertical  $z$  direction based on the higher resolution afforded in the vertical grid versus the horizontal grid in the model ABL.

From  $C_n^2(x, y, z, t)$ , we can derive estimates of attenuation due to scintillations based on Rytov theory (David, 2004; Clifford and Strohbehn, 1970). This theory holds for plane waves propagating through weak turbulence characterized by a Rytov Index ( $\sigma_\chi^2$ ), or scintillation variance, of less than 0.5 (David, 2004). The size scale of turbulent eddies in which Rytov theory finds applicability ranges from the inner scale, on the order of mm, to the outer scale, on the order of m, which defines the inertial sub-range of turbulence energy transport (Kaimal and Finnigan, 1994). Our particular case satisfies Rytov theory constraints in both the Rytov index ( $\sim 10^{-3} - 10^{-6}$ ) and size scale (vertical grid spacing  $\sim 10^1$  meters) as discussed in Section 3.1. We can then define our attenuation due to scintillations as follows (Clifford and Strohbehn, 1970):

$$A_{C_n^2} = 2 \cdot \sigma_\chi^2, \quad (3)$$

where the Rytov index is prescribed by:

$$\sigma_\chi^2 = 0.31 \cdot k^{7/6} \cdot L^{11/6} \cdot C_n^2. \quad (4)$$

In equation (4),  $k (=2\pi f/c; f=\text{frequency}, c=\text{speed of light})$  is the EM signal wavenumber and  $L$  is the signal propagation distance. We use a 1 km signal propagation length which yields attenuation values given in terms of decibels per kilometer (dB km<sup>-1</sup>). The attenuation contributions due to oxygen and water vapor ( $A_{O_2}, A_{H_2O}$ ) are also formulated to yield attenuation values in the same units.

Fig. 3 depicts specific attenuation contributions from scintillation and gaseous absorption for microwave EM frequencies ranging from 1 to 1000 GHz. Oxygen and water vapor curves were computed using the ITU-R P.676-6 model where pressure is set at standard atmospheric pressure at sea level (1013 hPa) and water vapor density was held at a fixed value of 1 g m<sup>-3</sup>. The scintillation curve was computed using (3) where a fixed values of  $C_n^2 (= 10^{-13} \text{ m}^{-2/3})$  and  $L (= 1000 \text{ m})$  were used. Microwave absorption by water vapor is characterized by peaks centered at specific frequencies including 22.2 GHz, 183.3 GHz, and 325.1 GHz and are induced by electric dipole transitions between varying rotational states within the water vapor molecules. Molecular oxygen possesses absorption peaks induced by electron spin dipole transitions centered at 60 GHz and 118.7 GHz.

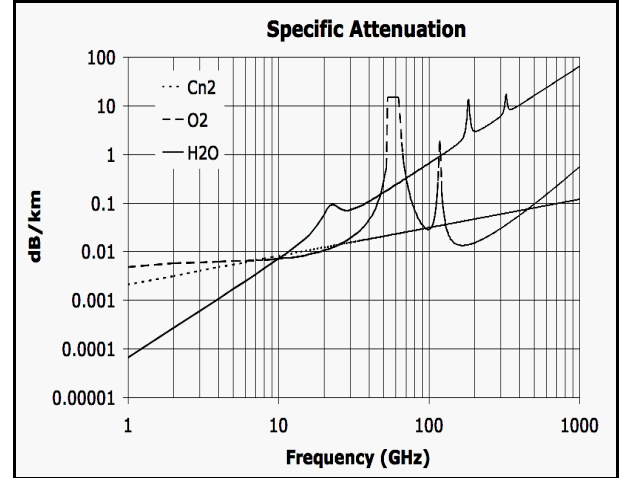


Fig. 3. Specific attenuations spectra for scintillations (Cn2), Oxygen (O2), and water vapor (H2O).

Since 2003, previously under-utilized EM frequency bands clustered around 70, 80, and 90 gigahertz have been made available for commercial and government usage. With 5 GHz of bandwidth available at 70 and 80 GHz and 3 GHz of bandwidth available at 90 GHz, Gigabit per second or greater data rates may be achieved (Well, 2006). These frequency bands are essentially undeveloped and possess considerable potential in a broad range of applications including high-speed, point-to-point wireless local area networks, and broadband communications (Watson, 1991). Highly directional, “pencil-beam” signal characteristics permit systems operating at these frequencies to function in close proximity to one another without interfering (Well, 2006). This characteristic permits the development remote sensing, data transmission, communications and electronic warfare systems that will not obstruct the operation of other friendly battlefield electronic devices. Our analysis will focus on attenuation effects that may hamper the transmission of an 80 GHz signal which is one potential frequency with a gigabit data rate capability. We will also now employ the scintillation and gaseous absorption attenuation models described in this section in our validation.

### 3.1 Validation

In order to ascertain the skill with which WRF ARW was able to predict meteorological variables needed in the calculation of attenuations, we will focus on observational data collected during the T-REX. Among the instrument used during the IOP phases was the National Center for Atmospheric Research (NCAR) Integrated Sounding System (ISS) Multiple Antenna Radar Profiler (MAPR). (Cohn et al., 2001). This instrument is an advanced boundary layer wind profiler that is capable of sampling wind speeds and directions,

Table 2. ISS MAPR/WRF ARW sampling intervals.

Intensive Observati on Period	Sampling time interval	Number of profiles
1	17 Z March 2 - 11 Z March 3, 2006	6
2	17 Z March 5 - 2 Z March 7, 2006	12
3	14 Z March 9 - 17Z March 10, 2006	6
4	20 Z March 13 - 23 Z March 14, 2006	10
6	2 Z March 25 - 3 Z March 26, 2006	7
8	17 Z March 31 - 11 Z April 1, 2006	6
9	12 Z April 2 - 5 Z April 3, 2006	5
10	5 Z April 8 - 2 Z April 9, 2006	6
12	11Z April 11 - 20 Z April 11, 2006	3
13	20Z April 15 - 8 Z April 17, 2006	10
14	8 Z April 21 - 20 Z April 21, 2006	4
15	8 Z April 26 - 11 Z April 27, 2006	6

temperatures, pressures, mixing ratios, and other variables at time scales on the order of minutes and at vertical resolutions of less than 5 meters. The instrument's location remained fixed at the Independence, California gravel pit (36.7874° N, 118.176° W) from the inception to the end of the T-REX field campaign (Grubisic et al., 2004). The bulk of the data collected by the ISS MAPR instrument was screened for completeness. It is summarized in Table 2 and serves as the basis for our forecast verification.

Since forecast data products produced by WRF ARW and vertical profiles of measured fields recorded by the ISS MAPR instrument differ in dimension, resolution, and temporal sampling, a number of post-processing tasks were performed in order to facilitate a comparative analysis between both data sets. A bilinear interpolation scheme (Henmi, 2000) was used to adjust WRF ARW prognostic fields values to match the ISS MAPR location. WRF ARW output fields are stored on the commonly utilized  $\sigma$  coordinate system which represents vertical model grid discretizations as ratios between a reference pressure and pressures at each level of the model atmosphere. The ISS MAPR instrument records data on vertical altitude levels given in units of m ASL. This disparity was resolved with the application of a cubic spline interpolation utility that produced a uniform grid that extended from an altitude of 1260 m to 3000 m ASL. A 20 m vertical resolution approximates measured atmospheric turbulence outer scales (Kaimal and Finnigan, 1994) which is required by Rytov theory as mentioned in the discussion of the scintillation model (3).

### 3.2 Case Study: IOP 8

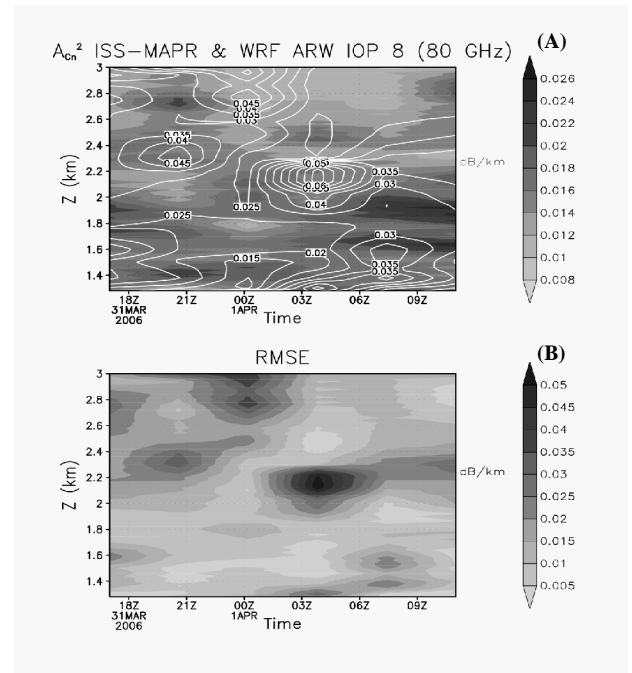


Fig. 4. IOP 8 time series profile for attenuation due to scintillations ( $A_{cn2}$ ); (A) is the baseline time series profile where shading represents ISS MAPR data and line contours represent WRF ARW data and (B) is the root mean squared error (RMSE) between ISS MAPR and TREX ARW data.

In order to isolate an ideal IOP case in which we can evaluate model forecast accuracy with respect to time and altitude, we examined time series statistics for each interval highlighted in Table 2. We found that WRF ARW and ISS MAPR time series profiles derived from IOP 8 possessed relatively low root mean square error (RMSE) values and high correlation coefficients (CCs) (not shown) as defined in the Appendix. Synoptic weather conditions during this period were dominated by a zone of low pressure to the north of the T-REX region accompanied by south-southeasterly flows. No precipitation was detected at any of the T-REX surface station locations including the ISS MAPR surface station. With a total of 6 ISS MAPR profiles sampled during this 18 hour period, we have a mean sampling interval of 3 hours which provides an adequate resolution in the time domain to examine the evolution of attenuation fields.

Fig. 4 depicts the attenuation time series profiles due to scintillations in which WRF ARW diagnostically-derived attenuations (white line contours) are superimposed on shaded ISS MAPR-derived measurements. Fig. 4 (A) demonstrates that WRF ARW and ISS MAPR attenuation profiles agreed poorly in terms of peak values ( $\sim 0.02$  dB  $\text{km}^{-1}$  for ISS MAPR and  $\sim 0.055$  dB  $\text{km}^{-1}$  for WRF ARW) and in overall pattern e.g. a conspicuous peak attenuation in the WRF ARW

profile occurred on April 1<sup>st</sup>, 2006 at ~03 Z and at a height of ~2.1 km ASL and is absent in the ISS MAPR profile. This level of attenuation in the ISS MAPR data would correspond to a ~0.5% loss in intensity for an 80 GHz signal that propagates over distance of 1 km. WRF ARW tends to over-predict the attenuation through this time period with a corresponding loss in signal intensity of 1.4%. Large RMSEs are evident in Fig. 4 (B) which further suggests that a poor agreement exists between model and observations for this specific IOP.

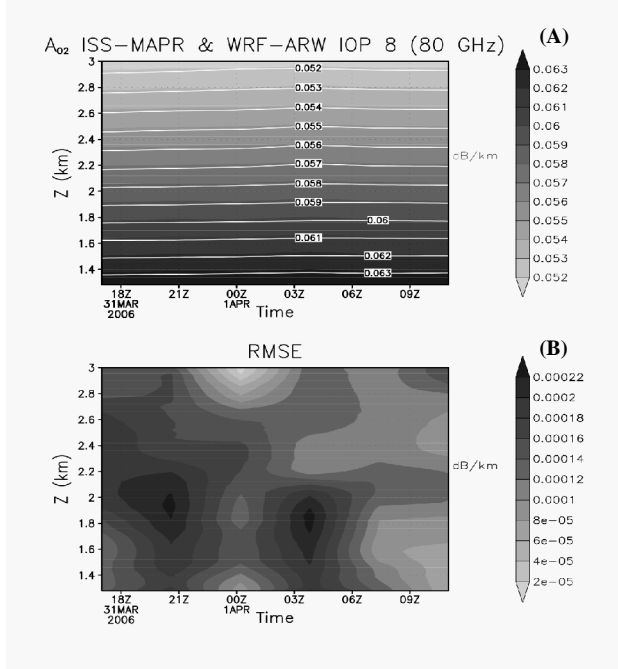


Fig. 5. IOP 8 time series profile for attenuation due to oxygen ( $A_{O_2}$ ); (A) is the baseline time series profile where shading represents ISS MAPR data and line contours represent WRF ARW data and (B) is the root mean squared error (RMSE) between ISS MAPR and TREX ARW data.

Fig. 5(A) presents time series profiles derived from attenuations driven by oxygen absorption. Noteworthy is the lack of variability during the IOP interval and the very good agreement between modeled and observed time series profiles. Since attenuation due to oxygen is modulated by oxygen partial pressure and frequency, it is not surprising that high CC values in pressure between both modeled and observed fields (Section 3.3) propagate forward into the calculation of attenuation. The RMSE time series profile (Fig. 5(B)) does reveal that small differences exist between WRF ARW and ISS MAPR baseline attenuations but these values are 3 orders of magnitude smaller than the baseline attenuations. A peak ISS MAPR attenuation of ~0.06 dB km<sup>-1</sup> corresponds to a loss in signal intensity of ~1.4% over 1 km of signal propagation distance. The combine contributions of both scintillations and oxygen attention would amount to ~0.08 dB km<sup>-1</sup> using ISS MAPR data and ~0.12 dB km<sup>-1</sup> using WRF ARW data. Although

these are not large attenuations, they may become significant for 80 GHz signals propagating at distances of 10 km or more.

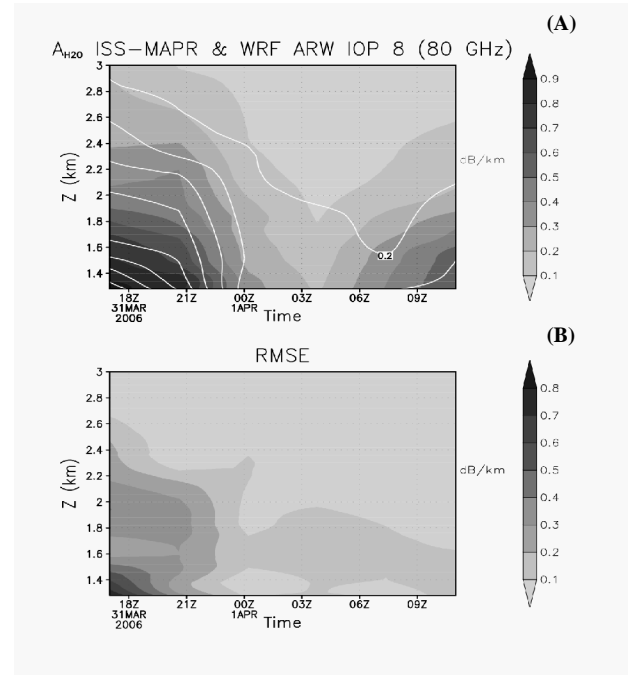


Fig. 6. IOP 8 time series profile for attenuation due to oxygen ( $A_{H_2O}$ ); (A) is the baseline time series profile where shading represents ISS MAPR data and line contours represent WRF ARW data and (B) is the root mean squared error (RMSE) between ISS MAPR and TREX ARW data.

The water vapor attenuation time series profile is depicted in Fig. 6(A). Two peaks in attenuation are noted ~1.8 km ASL and are clustered around 18Z on March 31, 2006 and 11 Z on April 1, 2006. These features suggest that the ABL has been moistened twice during IOP 8 and that the increase in water vapor density during these episodes had a direct effect on the attenuation of the 80 GHz signal. It was found that WRF ARW over-predicted the attenuation by roughly a factor of two compared to the peak attenuation realized in the ISS MAPR time series profile (~1 dB km<sup>-1</sup>). The corresponding loss in signal intensity for both data sets ranges from ~37% to ~21%, respectively.

The RMSE (Fig. 6(b)) time series profile suggests that the bulk of the difference between model and observation is attributable to the first incidence of ABL water vapor density increase. However, relatively good agreement between the two data sources is evident during the remainder of the IOP. When the baseline profiles are differenced and averaged vertically and in time, the resulting CC calculation yields a value of ~0.77. Overall, it is evident that water vapor attenuation would be the major contributing factor in signal degradation. With ISS MAPR values that range from 0.1

dB km<sup>-1</sup> to 1 dB km<sup>-1</sup>, it is clear that being able to accurately predict the water vapor content of the ABL would be a prerequisite in developing and implementing an accurate total attenuation forecast.

### 3.3 Results

A summary of ISS MAPR and WRF ARW IOP time series statistics is presented in Table 3. For each IOP interval, vertical profiles of several prognostic variables measured at ISS MAPR location were compiled. Statistical parameters computed in this comparison include RMSEs and CCs. These results were obtained by vertically averaging profile differences for each prognostic and diagnostic variable and then averaging over the time for the duration of each IOP presented in Table 2. The RMSE values for wind fields (u,v,ws) suggest that the model had no preferential skill in forecasting zonal or meridional winds and this is reinforced by the relatively low CC numbers. Wind fields are particularly difficult to predict as is the case in nearly all NWP validation studies.

The potential temperature ( $\theta$ ) prediction yielded a low RMSE value and a moderate CC compared with the wind fields. The relatively good agreement in potential temperature propagates into the calculation of ( $A_{Cn2}$ ). By far, WRF ARW did the best job in predicting pressure fields with a very low RMSE of 1.4 hPa and a CC of 0.96. This high correlation is reflected in a number of fields that possess a pressure dependence including index of refraction ( $n$ ), and attenuation due to oxygen absorption ( $A_{O2}$ ). Atmospheric mixing ratios (from which water vapor density,  $q$ , values are derived), reveal a moderate correlation and a relatively low RMSE of  $\sim 0.37$  g m<sup>-3</sup>. This statistical relationship in model versus observed water vapor density is also reflected in the calculation of attenuation due to water vapor absorption.

WRF ARW performed poorly in forecasting the refractive index structure parameter ( $C_n^2$ ) as its CC value is the lowest among the attenuation fields. This low correlation is reflected in the calculation of attenuation due to scintillations ( $A_{Cn2}$ ). Overall, the WRF ARW and ISS MAPR statistical comparison suggests that moderate to good predictive skill may be achieved in attempting to forecast EM signal attenuation effects with explicit dependence on pressure and moisture but the difficulty in accurately modeling scintillations effects hampers efforts in quantifying their contribution in total EM signal attenuation sources.

## CONCLUSIONS

Communication and remote sensing systems relying on microwave signal propagation may be impacted by

Table 3. ISS MAPR /WRF ARW statistical comparison for T-REX IOPs.

Comparison variable	RMSE	CC
u (zonal wind - m s <sup>-1</sup> )	2.14	0.25
v (meridional wind - m s <sup>-1</sup> )	2.30	0.27
ws (wind speed - m s <sup>-1</sup> )	2.66	0.20
$\theta$ (potential temperature - K)	1.44	0.55
p (pressure – hPa)	1.41	0.96
q (water vapor density - g m <sup>-3</sup> )	0.37	0.41
n (index of refraction)	1.74E-5	0.86
$C_n^2$ (refractive index structure parameter m <sup>-2/3</sup> )	1.25E-13	0.12
$A_{Cn2}$ (attenuation due to scintillations – dB km <sup>-1</sup> ) 80 GHz EM signal	0.01	0.12
$A_{O2}$ (attenuation due to oxygen absorption - dB km <sup>-1</sup> ) 80 GHz EM signal	1.02E-4	0.96
$A_{H2O}$ (attenuation due to water vapor absorption - dB km <sup>-1</sup> ) 80 GHz EM signal	0.17	0.41

conditions in the ABL through attenuations generated by turbulence (scintillations) and gaseous absorption. Multi-gigabit communications and remote sensing systems may be particular vulnerable to attenuation effects since they operate at 70-90 GHz frequencies where the combined effect of scintillations and gaseous absorption become significant. A comparison of high resolution, NWP forecast results (WRF ARW) and radar profiler (ISS MAPR) data derived from T-REX IOPs yielded good agreement in oxygen (CC= $\sim 0.96$ ) and water vapor (CC= $\sim 0.41$ ) attenuation predictions but diminished agreement in attenuations driven by scintillations (CC= $\sim 0.12$ ).

This results suggests that mesoscale NWP codes may be able to model ABL physical processes with sufficient accuracy to produce “propagation forecasts” (Hodges et al., 2006) that could be used to inform troops in the battlefield of how weather conditions within an area may impact communication and remote sensing systems operating at microwave frequencies. Future work will focus on including other sources of EM signal attenuation including hydrometeors and fog during T-REX and other observational field campaigns. Furthermore, future, in-situ, validation efforts which measure microwave signal losses within the battlefield environment could further assist in developing this approach.

## APPENDIX

The statistical parameters root mean square error (A1) and correlation coefficient (A2) were computed for variables displayed in Table 3. They take the same general form as presented in Henmi (2000):



$$\text{RMSE} = \sqrt{\frac{\sum_{j=1}^n \sum_{i=1}^m (x_{o,i,j} - x_{f,i,j})^2}{m \cdot n}}, \quad (\text{A1})$$

$$\text{CC} = \frac{\sum_{j=1}^n \sum_{i=1}^m (x_{o,i,j} - \bar{x}_o)(x_{f,i,j} - \bar{x}_f)}{\sqrt{\sum_{j=1}^n \sum_{i=1}^m (x_{o,i,j} - \bar{x}_o)^2 (x_{f,i,j} - \bar{x}_f)^2}}, \quad (\text{A2})$$

where  $x$  is a meteorological variable, indices  $f$ ,  $o$ ,  $z$ ,  $t$  designate (f)orecast data, (o)bservational data, (z) altitude, (t) time,  $m$  is the total number of altitude increments in the vertical coordinate, and  $n$  is the total number of time increments within the series.

### ACKNOWLEDGEMENTS

This study was funded, in part, by Army Research Laboratory Contract DAAD19-03-D-0001. We would like to thank James Doyle of the Naval Research Laboratory for guidance in developing the WRF ARW nested domain configuration and Bill Brown of the National Center for Atmospheric Research for access to ISS MAPR data.

### REFERENCES

- Bohlander, R. A., McMillan, R. W., Patterson, E. M., Clifford, S. F., Hill, R. J., Priestly, J. T., and Schoenfeld, W. P., 1988: Fluctuations in Millimeter Wave Signals Propagated Through Inclement Weather, *IEEE Trans. Geosci. Remote Sensing*, **26**, 343-354.
- Clifford, S. F., and Strohbehn, J. W., 1970: The Theory of Microwave Line-of-Sight Propagation Through a Turbulent Atmosphere, *IEEE Trans. Antennas Propag.*, **2**, 204-274.
- Cohn, S.A., Brown, W.O.J., Martin, C.L., Susedik, M.E., Maclean, G., and Parsons, D.B., 2001: Clear Air Boundary Layer Spaced Antenna Wind Measurement with the Multiple Antenna Profiler (MAPR), *Ann. Geophys.*, **19**, 845 - 854.
- David, F., 2004: Atmospheric Turbulence Monitoring at DLR, *Optics in Atmospheric Propagation and Adaptive Systems, Proc. of SPIE*, **5572**, 10-23.
- Grubisic, V., Doyle, J. D., Kuettner, J., Poulos, G. S., and Whiteman, C. D., 2004: *T-REX Terrain-Induced Rotor Experiment Overview Document and Experiment Design*.
- Henmi, T., 2000: Comparison and Evaluation of Operational Mesoscale MM5 and BFM Over WSMR, ARL-TR-1476.
- Hill, R. J., Bohlander, R. A., Clifford, S. F., McMillan, R. W., Priestley, J. T., Schoenfeld, W. F., 1988: Turbulence-Induced Millimeter-Wave Scintillations Compared with Micrometeorological Measurements, *IEEE Trans. Geosci. Remote Sensing*, **26**, 330-342.
- Hodges, D. D., Watson, R. J., and Wyman, G., 2006: An Attenuation Time Series Model for Propagation Forecasting, *IEEE Trans. Antennas Propag.*, **54**, 1726-1733.
- Hodur, R. M., 1997: The Naval Research Laboratory's Coupled Ocean/Atmosphere Mesoscale Prediction System (COAMPS), *Mon. Wea. Rev.*, **125**, 1414-1430.
- ITU-R P. 676-6, 2005: Attenuation by Atmospheric Gases.
- Kaimal, J. C., and Finnigan, J., 1994: *Atmospheric Boundary Layer Flows*, Oxford Univ. Press, New York.
- Kravtsov, Y. A., 1992: Propagation of Electromagnetic Waves Through a Turbulent Atmosphere, *Rep. Prog. Phys.*, 39-112.
- Meys, T., 2002: Modeling the Weather on the AHPCRC Cray X1, *AHPCRC Bull.*, **12**, 1-11.
- Muschinski, A., Sullivan, P. P., Wuertz, D. B., Hill, R. J., Cohn, S. A., Lenschow, D. H., and Doviak, R. J., 1999: First Synthesis of Wind-Profiler Signals on the Basis of Large-Eddy Simulation Data, *Radio Sci.*, **34**, 1437-1459.
- NMC Development Division, 1988: *Documentation of the research version of the NMC Medium-Range Forecasting Model*. NMC Development Division, Camp Springs, MD.
- Skamarock, W. C., Klemp, J. B., Dubhia, J. B., Gill, D. O., Barker, D. M., Wang, W., and Powers, J. G., 2005: *A Description of the Advanced Research WRF Version 2*, NCAR/TN-468+STR.
- Smith, E. K., 1982: Centimeter and Millimeter Wave Attenuation and Brightness Temperature due to Atmospheric Oxygen and Water Vapor, *Radio Sci.*, **17**, 1455-1464.
- Watson, P.A., 1991: Modelling Radio Propagation at Millimetre-Wavelengths For Communications and Remote Sensing, *IEEE Trans. Antennas Propag.*, ICAP 91., Seventh International Conference, 269-273.
- Wells, J., 2006: Multigigabit Wireless Technology at 70 GHz, 80 GHz, and 90 GHz, *RF Des.*, 50-54.

# Mesoscale Forecast Analysis of Atmospheric Boundary Layer Structure and Electromagnetic Signal Attenuation During the Terrain-Induced Rotor Experiment (T-REX)

Edward Colón

Network Computing Services, Inc. / Army High Performance Computing Research  
Center, Adelphi, Maryland, 20783

Robert E. Dumais, Teizi Henmi, and Robert Flanigan

Army Research Laboratory / Battlefield Environment Division White Sands Missile  
Range, New Mexico, 88062



Approved for Public Release  
Copyright NCSI



Army High Performance Computing Research Center  
Support Infrastructure Contract  
Network Computing Services, Inc. , Prime Contractor  
Contract DAAD19-03-D-0001

This presentation was developed in connection with contract DAAD19-03-D-0001 with the U.S. Army Research Laboratory. The views and conclusions contained in this presentation are those of the authors and should not be interpreted as presenting the official policies or positions, either expressed or implied, of the U.S. Army Research Laboratory or the U.S. Government unless so designated by other authorized documents. Citation of manufacturer's or trade names does not constitute an official endorsement or approval of the use thereof.

The U.S. Government is authorized to reproduce and distribute reprints for Government purposes notwithstanding any copyright notation hereon.



Approved for Public Release  
Copyright NCSI



# Objectives

- Our goal is to ascertain the skill with which we can predict ABL conditions and quantify their impact on the propagation of EM signals that are vulnerable to scintillation and gas absorption attenuation effects.
- We describe the implementation of WRF ARW in support of Terrain-Induced Rotor Experiment (T-REX) from which we derive high resolution numerical weather prediction model forecast results and attenuation fields using diagnostic models.
- A statistical comparison between WRF ARW-derived attenuation fields and Integrated Sounding System (ISS) Multiple Antenna Profiling Radar (MAPR)-derived attenuation fields is presented.

# Relevance



BBC



Army



Army

- **Microwave Attenuation (1-1000 GHz)**

## Consequences:

- Communication system fidelity and range.
- Targeting system tracking errors.
- High bandwidth data transmission fidelity and range.

## Principal Causes:

- Gaseous absorption ( $O_2$ ,  $H_2O$ )
- Turbulence-driven fluctuations in atmospheric index of refraction (scintillations)
- Incoherent scatterers (aerosols, hydrometeors)
- Coherent scatterers (man-made structures)

# T-REX

- Science campaign exploring the structure & evolution of atmospheric rotors.
  - Participants included several research agencies and academic institutions
  - Domain: Owens Valley, CA and the surrounding region.
  - Duration: March 1, 2006 – May 1, 2006.
- ARL/AHPCRC Contribution:
- Near Real-time WRF ARW 48-hour, daily forecast products available at:

<http://catalog.eol.ucar.edu/cgi-bin/trex/model/index>

- The AHPCRC Cray X1E served as the primary HPC workhorse.
- Forecast products generated daily from 12Z February 28, 2006 to 12Z May 2, 2006 for a total of 62 overlapping 48-hour cycles.

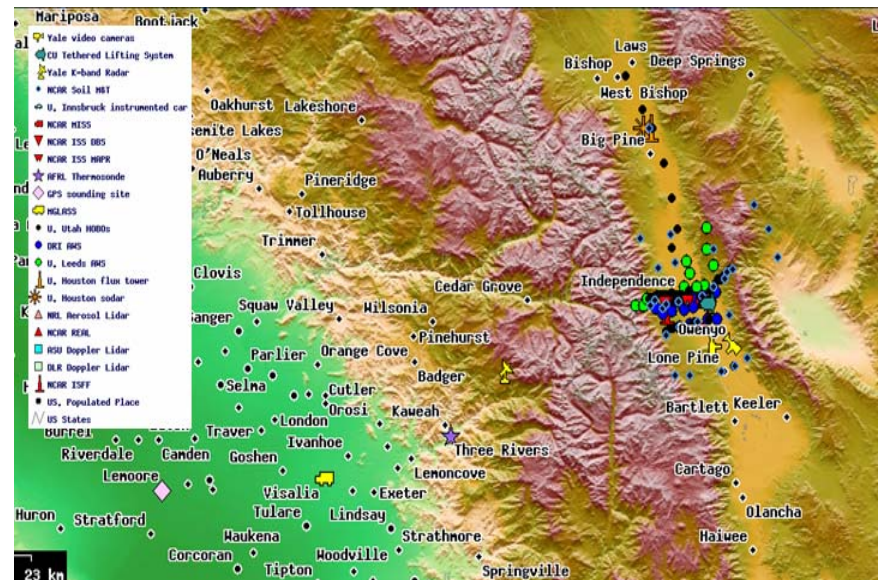


Fig. 1. T-REX domain and observing station network.

# WRF ARW Domains

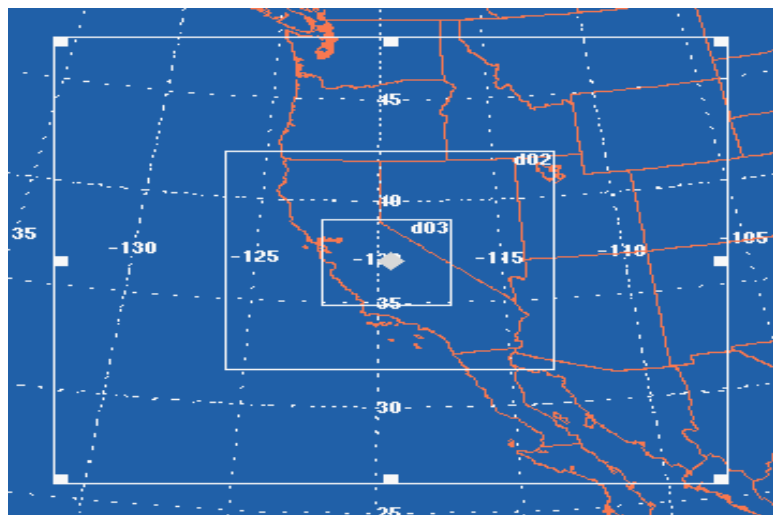


Fig. 2. WRF ARW nested domain configuration

- Initialized using a “cold start” condition with Global Forecasting System (GFS) 0.5° resolution data.
- Outermost domain: 91 X 91 grid elements with an 18 km resolution
- First nested domain: 157 X 157 grid elements with a 6 km resolution

- Innermost domain: 133 X 133 grid elements with a resolution of 2 km.
- 40 vertical levels defined in each domain distributed from the model surface to a 10 hPa model top.

Table 1. Model Configuration

Physics scheme/parameterization	WRF -AR W
Microphysics	Lin et al.
Cumulus physics	Kain-Fritsch scheme
Shortwave radiation	Dudhia scheme
Longwave radiation	Rrtm scheme
Land surface model	NOAH model
ABL/surface similarity scheme	YSU scheme
Surface layer physics	Monin-Obukhov scheme
Time step-to-resolution ratio	3:1
Domain nesting ratio	3:1
Nesting scheme	Interactive



# WRF ARW Validation

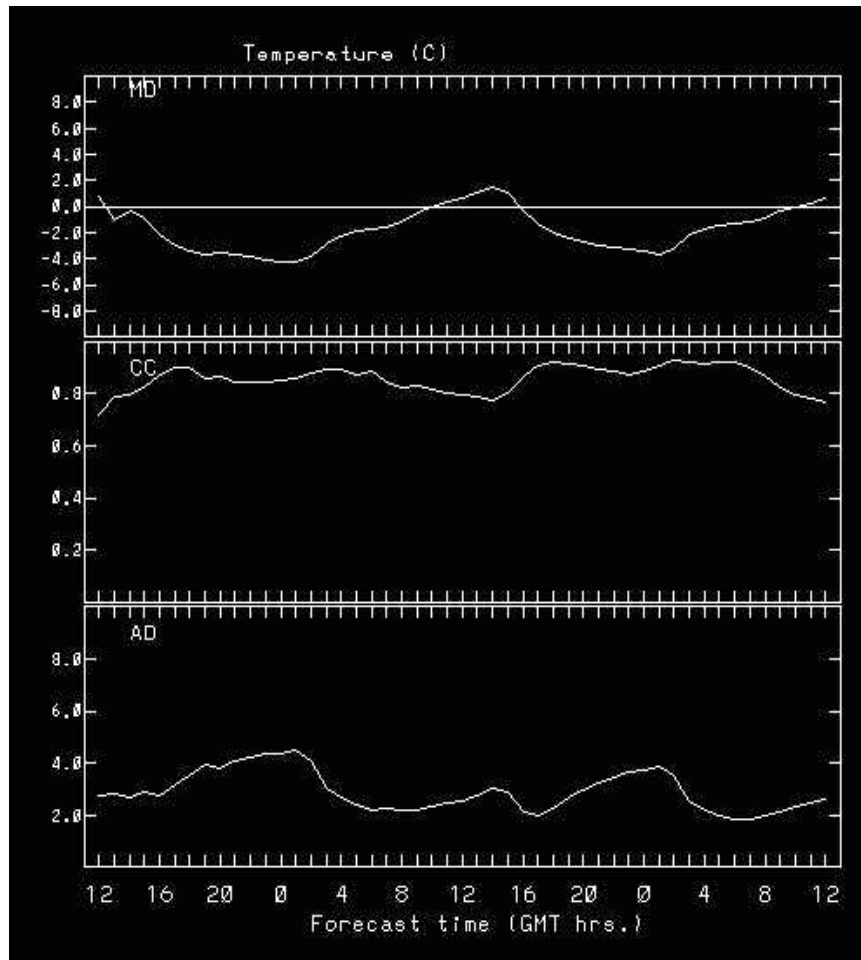


Fig. 3. Mean Difference (MD), Correlation Coefficient (CC), and Absolute Difference (AD) for temperature.

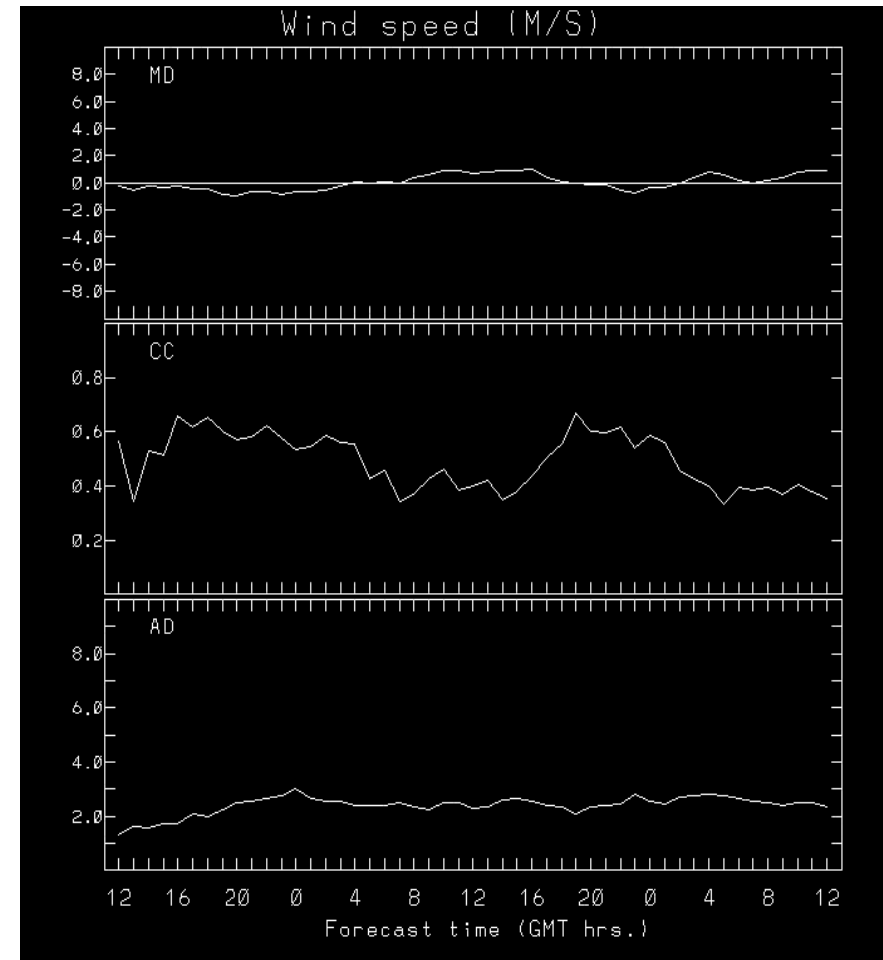


Fig. 4. Mean Difference (MD), Correlation Coefficient (CC), and Absolute Difference (AD) for wind speed.



# EM Signal Propagation Forecasting

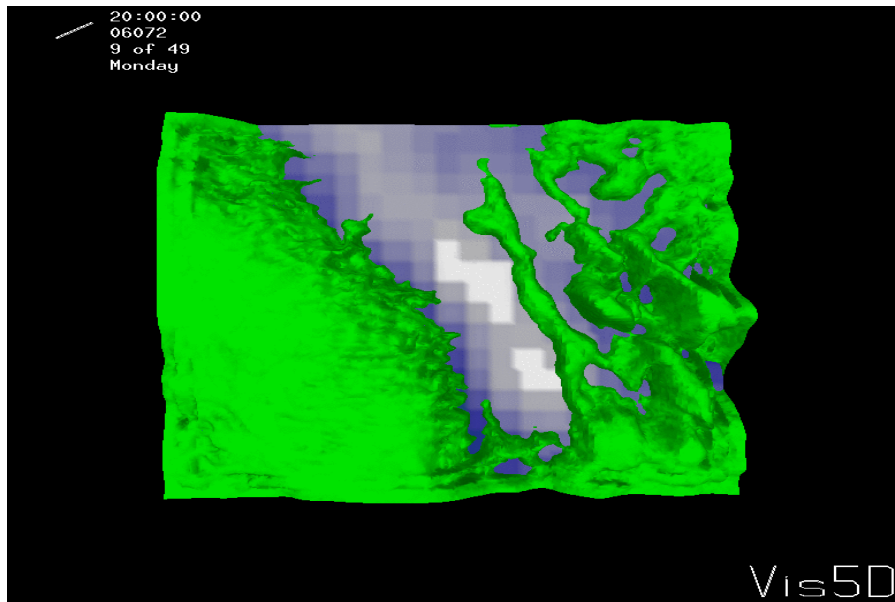


Fig. 5. Refractive index isosurface ( $2.5 \times 10^{-4}$ ).

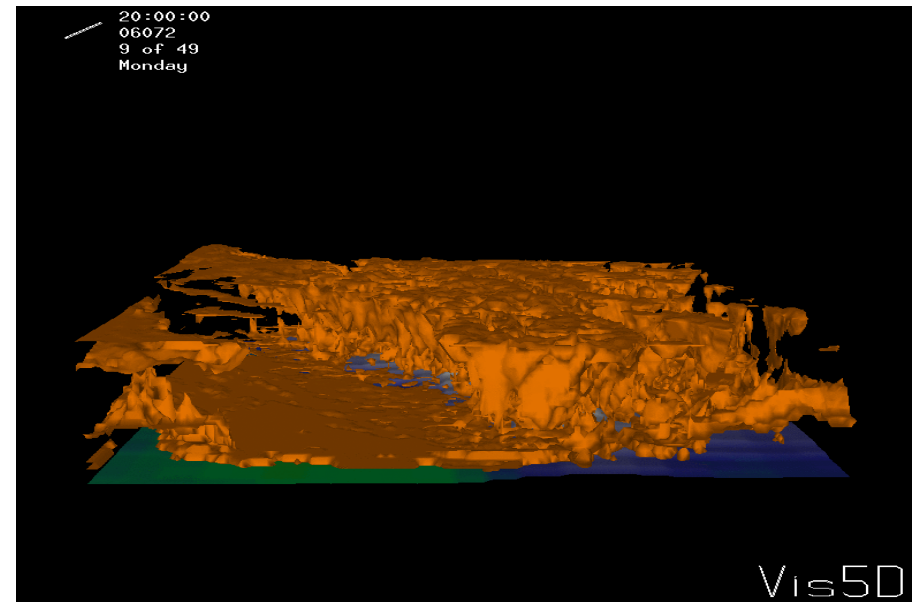


Fig. 6.  $C_n^2$  isosurface ( $2 \times 10^{-12} \text{ m}^{-2/3}$ ).

$$n(x,y,z,t) = C \frac{P(x,y,z,t)}{\theta(x,y,z,t)} + C_w \frac{e(x,y,z,t)}{\theta(x,y,z,t)^2}$$

where  $C = 7.76 \times 10^7 \text{ K Pa}^1$ ,  $C_w = 3.73 \times 10^3 \text{ K}^2 \text{ Pa}^{-1}$ ,  $(x,y,z,t)$  cartesian coordinates are  $P(x,y,z,t)$  is total atmospheric pressure,  $\theta(x,y,z,t)$  is potential temperature,  $e(x,y,z,t)$  is water vapor pressure

$$C_n^2(x,y,z,t) = \frac{[n(x,y,z + \Delta z/2,t) - n(x,y,z - \Delta z/2,t)]^2}{\Delta z^{2/3}}$$

where  $\Delta z$  is the vertical grid spacing

# EM Signal Propagation Forecasting

## • Attenuation models:

### Oxygen [ITU-R P.676]

when  $f < 57$  GHz

$$A_{O_2} = \left[ (0.00719) + \frac{6.09}{f^2 - 10.237} + \frac{4.81}{(f - 57)^2} \right] \cdot f^2 \cdot 10^{-4} \text{ dB km}^{-1}$$

when  $f > 63$  GHz

$$A_{O_2} = \left[ (3.79 \cdot 10^{-7} \cdot f) + \frac{0.625}{(f - 63)^2 + 1.59} + \frac{0.028}{(f - 118)^2 + 1.47} \right] \cdot (f + 198)^2 \cdot 10^{-3} \text{ dB km}^{-1}$$

when  $57 \text{ GHz} < f < 63 \text{ GHz}$

$$A_{O_2} = 14.9 \text{ dB km}^{-1}$$

### Water Vapor [ITU-R P.676]

$$A_{H_2O} = \left[ (0.05 + 0.021) \cdot \rho_{H_2O} + \frac{3.6}{(f - 22.2)^2 + 8.5} + \frac{10.6}{(f - 183.3)^2} + \frac{8.9}{(f - 325.4)^2 + 26.3} \right] \cdot f^2 \cdot \rho_{H_2O} \cdot 10^{-4} \text{ dB km}^{-1}$$

where  $f$  is the frequency of the propagating EM signal (GHz) and  $H_2O$  is water vapor density ( $\text{g m}^{-3}$ ).

# EM Signal Propagation Forecasting

## Scintillations (turbulence) [David, 2004]

$$A_{C_n^2} = 2 \cdot \sigma_\chi^2,$$

where

$$\sigma_\chi^2 = 0.31 \cdot k^{7/6} \cdot L^{11/6} \cdot C_n^2$$

and  $k$  ( $=2\pi f/c$ ;  $f$ =frequency,  $c$ =speed of light) is the EM input signal wavenumber,  $L$  is the signal propagation distance, and  $C_n^2$  is the refractive index structure parameter computed from index of refraction diagnostic fields derived from model and observational data sets.

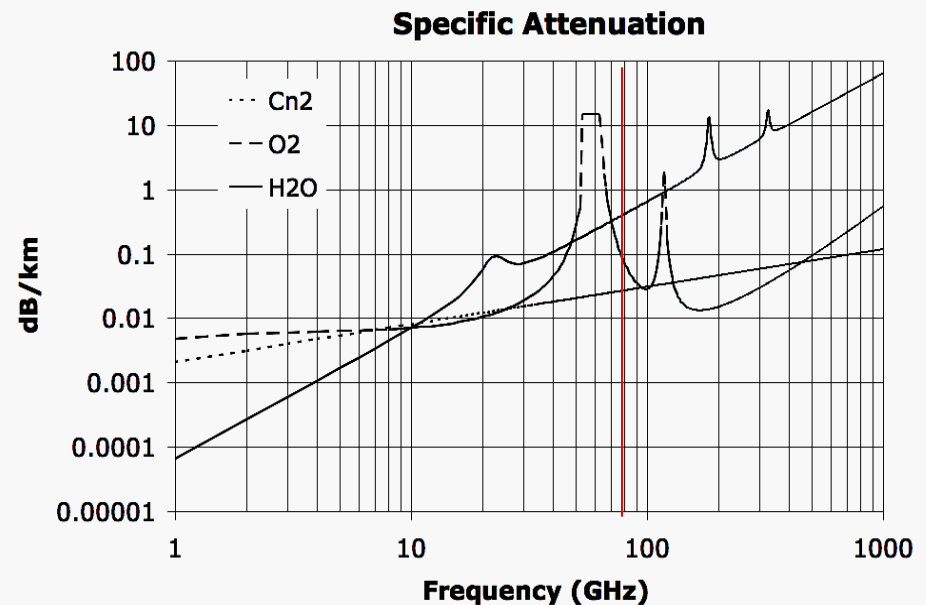


Fig. 7. Specific attenuations spectra for scintillations (Cn2), Oxygen (O2), and water vapor (H2O). Red line corresponds to 80 GHz (multi-bit frequency).

- Cn2 is fixed at :  $10E-13$
- Water vapor density is fixed at  $1 \text{ g m}^{-3}$
- Pressure is the US standard atmosphere pressure at the surface (1013 hPa).
- Temperature is the US Standard atmosphere at the surface

# EM Signal Propagation Forecast Validation



MAPR (Multiple Antenna Profiler Radar) was developed at NCAR (National Center for Atmospheric Research) /EOL (Earth Observing Laboratory)

- ISS MAPR profiles obtained during T-REX IOPs at the Independence, California gravel pit (36.7874° N, 118.176° W, 1202 m ASL)

- WRF ARW and ISS MAPR data were interpolated onto a 20 meter resolution vertical grid extending from 1200 m ASL to 3000 m ASL.

- A 80 GHz EM signal was used in all attenuation calculations.

Table 2. T-REX IOP time periods and the associated ISS MAPR vertical profile records.

Intensive Observation Period	Sampling time interval	profiles
1	17 Z March 2 - 11 Z March 3, 2006	6
2	17 Z March 5 – 2 Z March 7, 2006	12
3	14 Z March 9 – 17Z March 10, 2006	6
4	20 Z March 13 – 23 Z March 14, 2006	10
6	2 Z March 25 – 3 Z March 26, 2006	7
8	17 Z March 31 – 11 Z April 1, 2006	6
9	12 Z April 2 – 5 Z April 3, 2006	5
10	5 Z April 8 – 2 Z April 9, 2006	6
12	11Z April 11 – 20 Z April 11, 2006	3
13	20Z April 15 – 8 Z April 17, 2006	10
14	8 Z April 21 – 20 Z April 21, 2006	4
15	8 Z April 26 – 11 Z April 27, 2006	6

# EM Signal Propagation Forecast Validation

Table 3. Root mean square Errors (RMSE) & Correlation Coefficients (CC) derived from vertically and temporally averaged WRF ARW and ISS MAPR data sets over all IOPs.

Comparison variable	RMSE	CC
u (zonal wind - $\text{m s}^{-1}$ )	$2.14 \pm 2.56$	$0.25 \pm 0.2$
v (meridional wind - $\text{m s}^{-1}$ )	$2.30 \pm 1.42$	$0.27 \pm 0.25$
ws (wind speed - $\text{m s}^{-1}$ )	$2.66 \pm 2.83$	$0.20 \pm 0.19$
$\theta$ (potential temperature - K)	$1.44 \pm 0.84$	$0.55 \pm 0.24$
p (pressure – hPa)	$1.41 \pm 0.70$	$0.96 \pm 0.004$
densw (water vapor density - $\text{g m}^{-3}$ )	$0.37 \pm 0.31$	$0.41 \pm 0.24$
n (index of refraction)	$1.74\text{E-}5 \pm 3.70\text{E-}6$	$0.86 \pm 0.07$
$C_n^2$ (refractive index structure parameter $\text{m}^{-2/3}$ )	$1.25\text{E-}13 \pm 3.43\text{E-}14$	$0.12 \pm 0.16$
$A_{\text{Cn}2}$ (attenuation due to scintillations – $\text{dB km}^{-1}$ ) 80 GHz EM signal	$0.01 \pm 0.002$	$0.12 \pm 0.16$
$A_{\text{O}_2}$ (attenuation due to oxygen absorption - $\text{dB km}^{-1}$ ) 80 GHz EM signal	$1.02\text{E-}4 \pm 5.04\text{E-}5$	$0.96 \pm 0.006$
$A_{\text{H}_2\text{O}}$ (attenuation due to water vapor absorption - $\text{dB km}^{-1}$ ) 80 GHz EM signal	$0.17 \pm 0.21$	$0.41 \pm 0.25$

# EM Signal Propagation Forecast Validation

## Case Study: IOP 8

- We found that WRF ARW and ISS MAPR time series profiles derived from IOP 8 possessed relatively low RMSE values and high CC's.
- Synoptic weather conditions during this period were dominated by a zone of low pressure to the north of the T-REX region accompanied by south-southeasterly flows.
- Active mountain wave and rotors but no measurable precipitation.

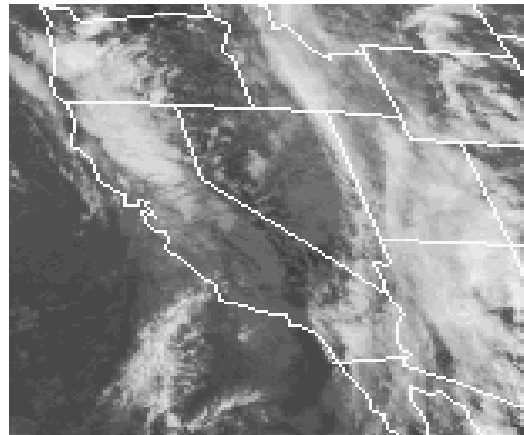


Fig. 8. GOES-W Infrared - 0Z April 1, 2006

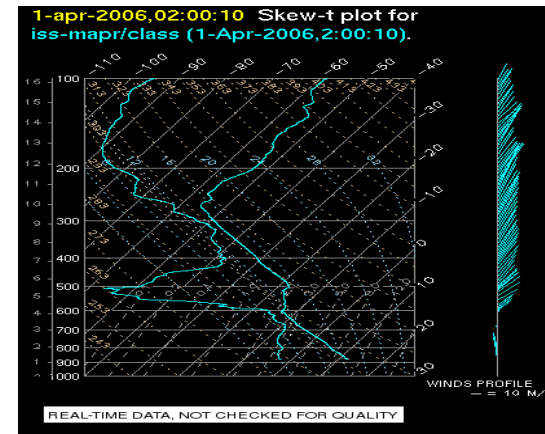


Fig. 9. ISS MAPR Skew-T - 0Z April 1, 2006

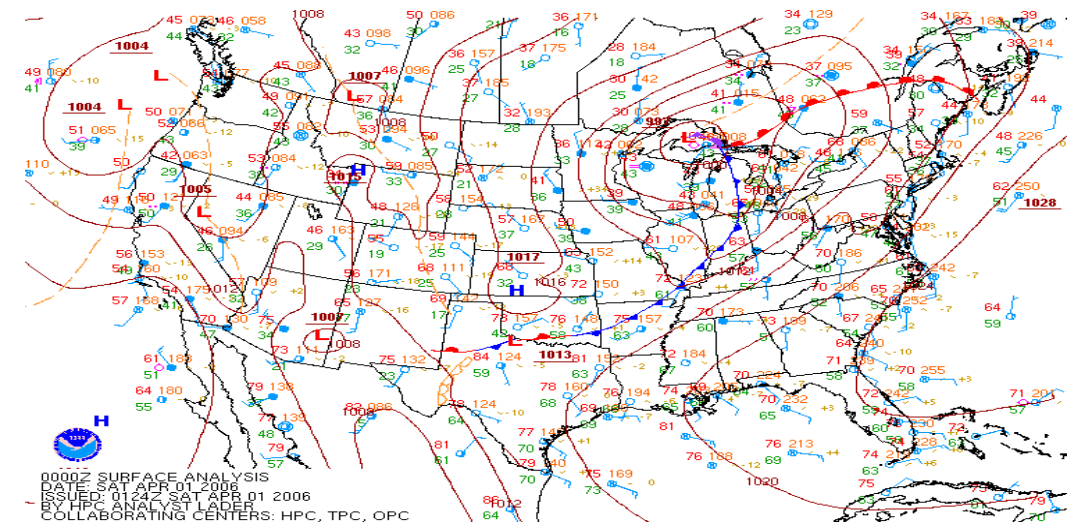


Fig. 10. NOAA surface analysis - 0Z April 1, 2006.

# EM Signal Propagation Forecast Validation

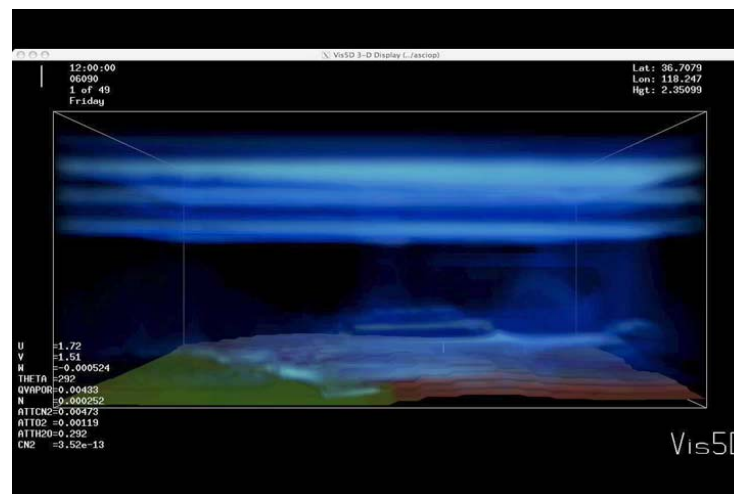


Fig. 11. IOP8 attenuation due to scintillations

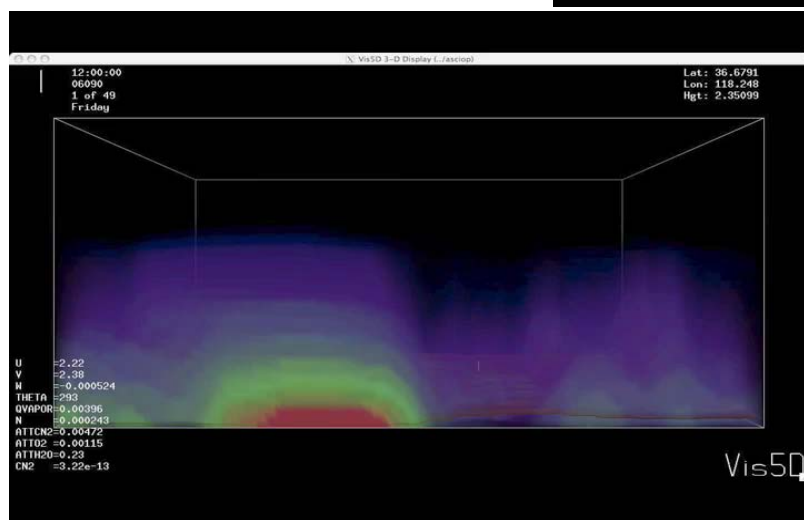


Fig. 12. IOP 8 attenuation due to oxygen

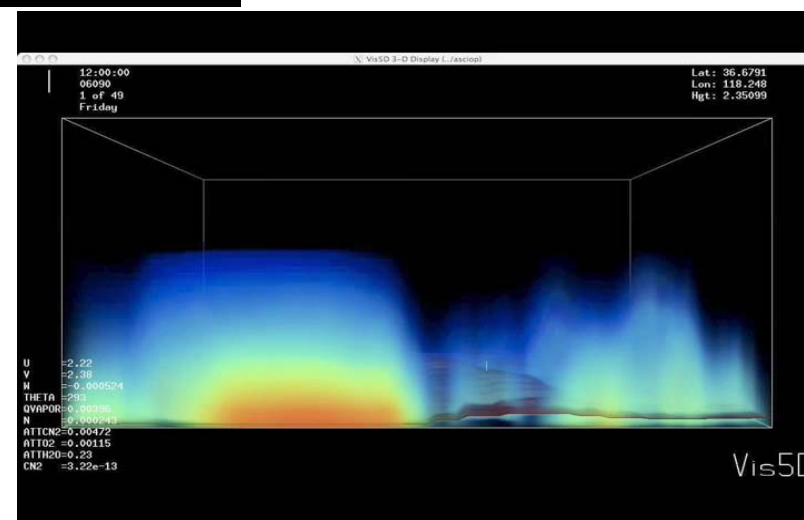


Fig. 13. IOP 8 attenuation due to water vapor



# EM Signal Propagation Forecast Validation

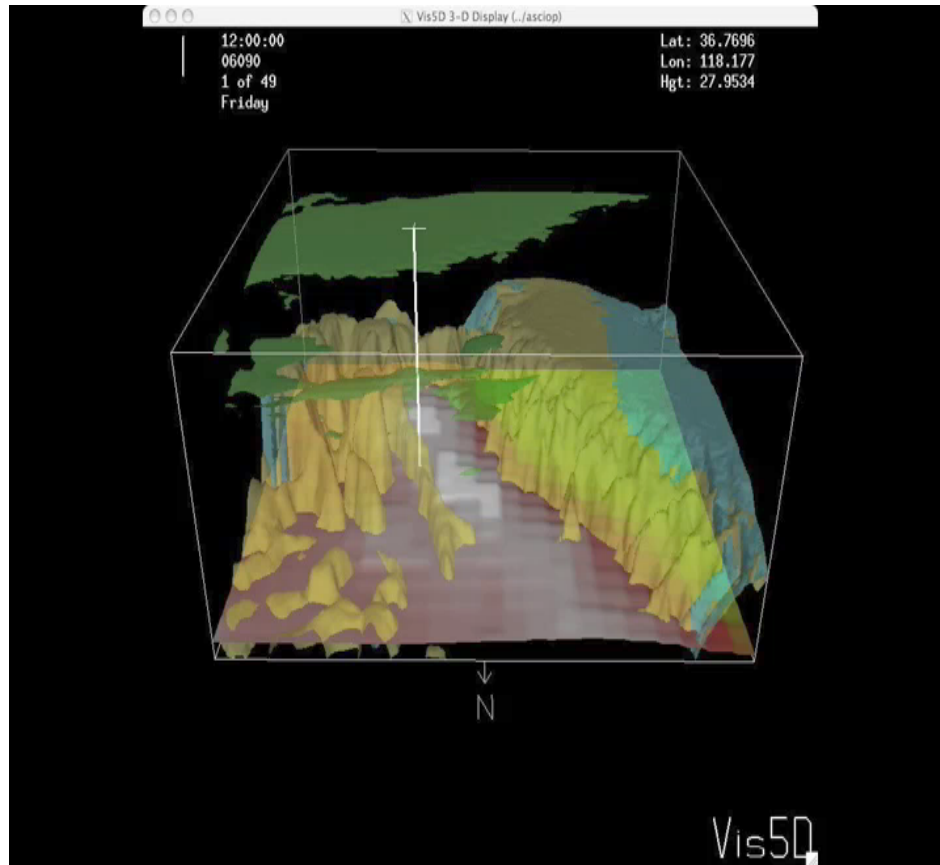


Fig. 14. IOP8 attenuations due to three sources (green: scintillations - 0.011 dB/km isosurface; blue: oxygen - 0.018 dB/km isosurface; yellow: water vapor - 0.35 db/km isosurface)

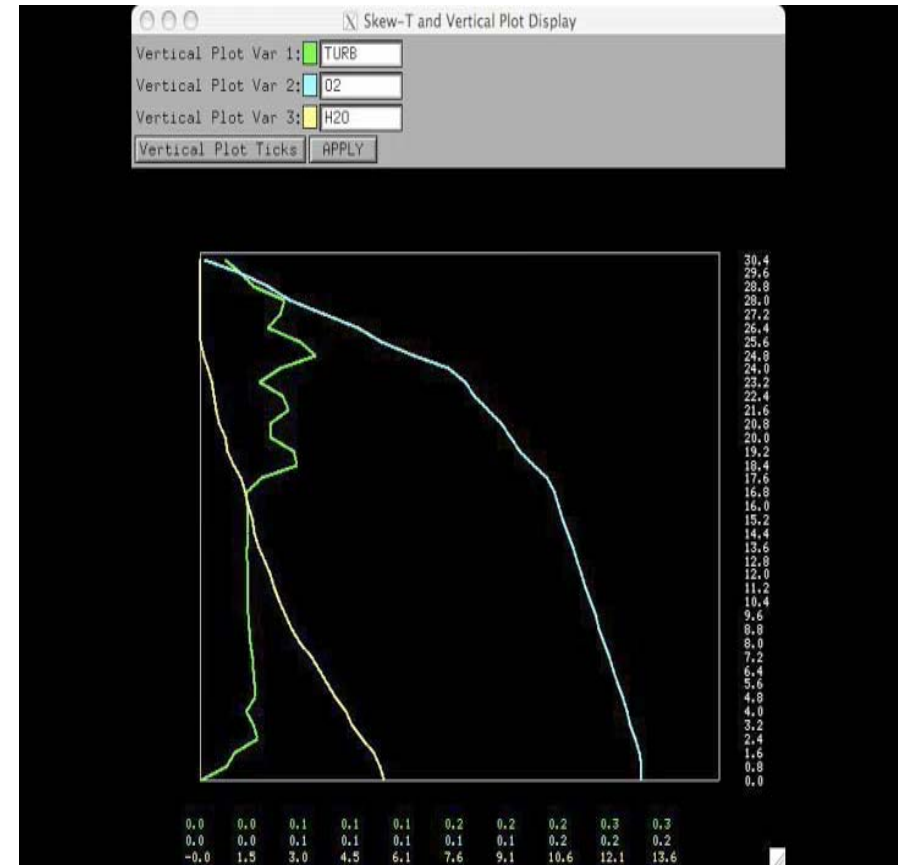


Fig. 15. IOP8 vertical attenuation profiles values (X10) due to three sources (green: scintillations; blue: oxygen; yellow: water vapor)



# EM Signal Propagation Forecast Validation

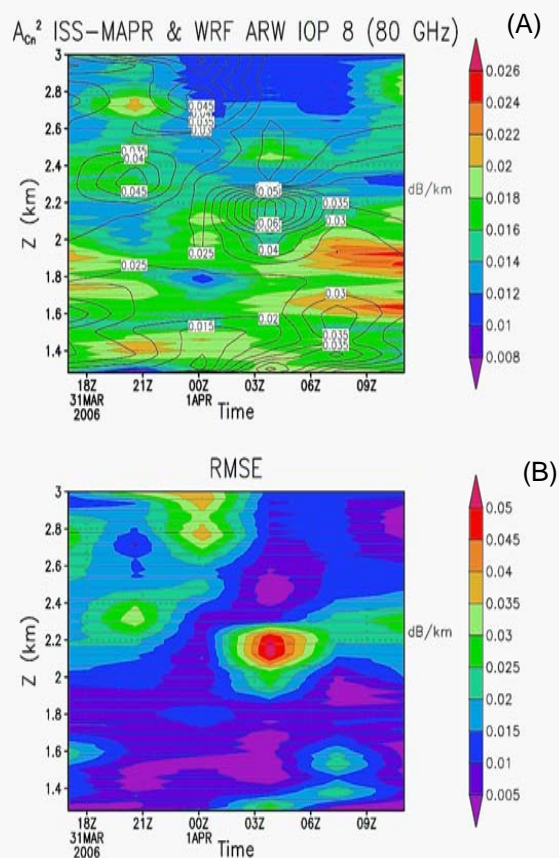


Fig. 16. IOP 8 time series profile for attenuation due to oxygen ( $A_{O_2}$ ); (A) baseline time series, (B) RMSE between ISS MAPR and TRES ARW data.

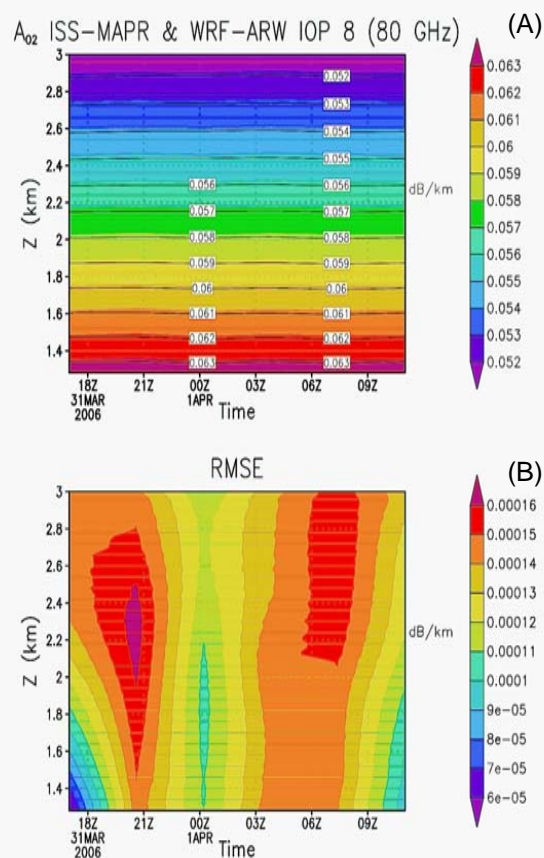


Fig. 17. IOP 8 time series profile for attenuation due to scintillations ( $A_{Cn2}$ ); (A) baseline time series, (B) RMSE between ISS MAPR and TRES ARW data.

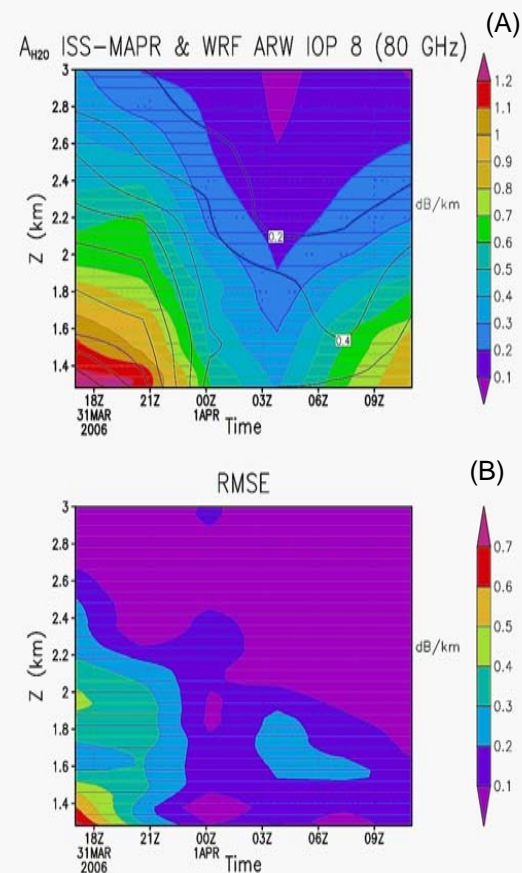


Fig. 18. IOP 8 time series profile for attenuation due to water vapor ( $A_{H_2O}$ ); (A) baseline time series, (B) RMSE between ISS MAPR and TRES ARW data.

# Summary

- Communication and remote sensing systems relying on microwave signal propagation may be affected by atmospheric conditions in the battle field ABL through attenuations generated by turbulence (scintillations) and gaseous absorption.
- Multi-gigabit communications and remote sensing may be particular vulnerable to attenuation effects since they operate at 70-90 GHz frequencies where the combined impact of scintillations and gaseous absorption become significant.
- A comparison of WRF ARW and ISS MAPR data derived from the T-REX IOPs yielded good agreement in oxygen ( $r \sim 0.96$ ) and water vapor attenuation ( $r \sim 0.41$ ) predictions but poor agreement in attenuations driven by scintillations ( $r \sim 0.12$ ).
- Estimated 80 GHz signal loss reached as high as ~37% during IOP 8 due to water vapor attenuations.
- Future work will focus on deriving total slant path signal attenuations for additional sources including hydrometeors and fog during T-REX.

# ACKNOWLEDGEMENTS

We would like to thank

- James Doyle of the Naval Research Laboratory for guidance in developing the WRF ARW nested domain configuration.
- Bill Brown of the National Center for Atmospheric Research for access to ISS MAPR data.

